

Theory of spin-selective Andreev reflection in the vortex core of a topological superconductor

Lun-Hui Hu,^{1,2} Chuang Li,^{1,2} Dong-Hui Xu,³ Yi Zhou,^{1,2,*} and Fu-Chun Zhang^{1,2,†}¹*Department of Physics, Zhejiang University, Hangzhou, Zhejiang, 310027, China*²*Collaborative Innovation Center of Advanced Microstructures, Nanjing 210093, China*³*Department of Physics, Hong Kong University of Science and Technology, Clear Water Bay, Hong Kong, China*

(Received 20 July 2016; revised manuscript received 21 October 2016; published 1 December 2016)

Majorana zero modes (MZMs) have been predicted to exist in a topological insulator (TI)/superconductor (SC) heterostructure. A recent spin-polarized scanning tunneling microscope (STM) experiment [Sun *et al.*, *Phys. Rev. Lett.* **116**, 257003 (2016)] has observed a spin-polarization dependence of the zero bias differential tunneling conductance at the center of a vortex core. Here, we consider a helical electron system described by a Rashba spin-orbit coupling Hamiltonian on a spherical surface with an s -wave superconducting pairing due to proximity effect. We examine the in-gap excitations of a pair of vortices with one at the north pole and the other at the south pole. While the MZM is not a spin eigenstate, the spin wave function of the MZM at the center of the vortex core, $r = 0$, is parallel to the magnetic field, and the local Andreev reflection of the MZM is spin selective, namely, occurs only when the STM tip has the spin polarization parallel to the magnetic field, similar to the case in a one-dimensional nanowire [He *et al.*, *Phys. Rev. Lett.* **112**, 037001 (2014)]. The total local differential tunneling conductance consists of the normal term proportional to the local density of states and an additional term arising from the Andreev reflection. We also discuss the finite size effect, for which the MZM at the north pole is hybridized with the MZM at the south pole. We apply our theory to examine the recently reported spin-polarized STM experiments and show good agreement with the experiments.

DOI: [10.1103/PhysRevB.94.224501](https://doi.org/10.1103/PhysRevB.94.224501)

I. INTRODUCTION

In condensed matter physics, Majorana [1] zero modes (MZMs) are a special type of Bogoliubov quasiparticle excitations with non-Abelian statistics, which have been proposed to be building blocks for quantum information and quantum computation [2,3]. There have been a number of theoretical proposals [4,5] to realize MZMs in condensed matter systems, such as a $\nu = 5/2$ fractional quantum Hall system [6], a chiral p -wave superconductor [7], topological insulator(TI)/ s -wave superconductor(SC) interfaces with MZM in the vortex core [8], proximity-induced superconductors for spin-orbit coupled nanowires [9,10], spin-orbit coupled semiconductors [11–13] with an externally applied Zeeman field, and ferromagnetic atoms in proximity to superconductors [14,15]. There also exist various experimental evidences for MZMs in these proposed systems [16–24].

Very recently, He *et al.* [25] have predicted that an MZM at the end of a nanowire may induce spin-selective Andreev reflection (SSAR). An electron with the same spin of the MZM will undergo an Andreev reflection, while an electron with opposite spin does not. This SSAR is a novel property of the MZMs and is different from the ordinary Andreev reflection (AR) [26–28]. This property may allow us to reveal the spin degrees of freedom of the MZMs. However, in 1D nanowire systems, it always requires a large Zeeman term to host MZMs, which may make it difficult to attribute the spin-polarization dependence to the MZMs.

Fu and Kane [8] proposed that MZMs are localized inside the vortex core in a TI/SC heterostructure, and they showed this explicitly by solving Bogoliubov-de Gennes equations (BdG) [29]. Experimentally, the MZMs in such a system have

been demonstrated by STM based on a zero-bias peak (ZBP) in a $\text{Bi}_2\text{Te}_3/\text{NbSe}_2$ heterostructure made of a TI thin film Bi_2Te_3 on the top of a NbSe_2 SC [21,23]. Most recently, strong new evidence for the MZM inside the vortex core is reported by using spin-polarized STM [30]. The experiment has clearly shown spin-polarization dependence of the differential tunneling conductance $dI/dV(E, r = 0)$. In this paper, we present a systematic model calculation to examine the SSAR inside the vortex core of TI/SC.

We consider a helical metal described by a Rashba spin-orbit coupling Hamiltonian on a spherical surface of radius R . Superconductivity is introduced by proximity effect and the electronic structure in a vortex state is studied. At the center of the vortex core, $r = 0$, the spin component of the MZM is parallel to the magnetic field, and the local Andreev reflection of the MZM is spin selective, and only occurs when the STM tip has the spin polarization parallel to the magnetic field. The first quasiparticle state has the same amplitude of orbital wave function with, but opposite spin polarization to the MZM at $r = 0$. This leads to approximately the same local density of states and normal differential tunneling conductance for the spin parallel and antiparallel to the magnetic field cases. We also discuss the finite size effect. We apply our theory to examine the recently reported spin-polarized STM experiments and show good agreement with the experiments.

The paper is organized as follows. In Sec. II, the BdG equation is introduced and we adopt spherical geometry to solve the eigenfunction problem. The numerical results are presented systematically in Sec. III. The method and results of the transport calculations for Andreev reflection (AR) at the center of the vortex core are discussed in detail in Sec. IV. A summary and conclusion are presented in Sec. V. In Appendix, the vortex-free BdG equation will be addressed and the well-known Blonder-Tinkham-Klapwijk (BTK) theory is reproduced by using our method.

*yizhou@zju.edu.cn

†fuchun@hku.hk

II. VORTEX STATES IN PROXIMITY-INDUCED TOPOLOGICAL SUPERCONDUCTOR ON SPHERICAL SURFACE

In this section, we discuss vortex states in a topological superconductor, which is modelled by a helical metal with proximity-induced superconductivity. The helical metal represents the surface states of a 3D topological insulator. We consider spherical geometry, in which electrons in the helical metal are confined on a spherical surface. In this geometry, the boundary is closed. We will start with a noninteracting electron system with a Rashba spin-orbit coupling, then discuss such a helical metal under the proximity effect of superconductivity in the absence of vortices. Finally, we will also discuss the in-gap vortex states of the system.

A. 2D Helical metal on a spherical surface

The surface state of a 3D topological insulator may be described by noninteracting helical electrons on the x - y plane. The single-electron Hamiltonian reads

$$\mathcal{H}_0 = \alpha(\boldsymbol{\sigma} \times \vec{p}) \cdot \vec{z} - \mu, \quad (1)$$

where α is the spin-orbit coupling strength, which will be assumed to be positive throughout this paper without loss of generality. $\vec{\sigma}$ is made of the three Pauli matrices, \vec{p} is the momentum confined in the x - y plane, and μ is the chemical potential. The Hamiltonian in the x - y plane can be generalized to a spherical surface of radius R , by using the expression $\vec{p} = -i[\vec{\nabla} - \hat{R}(\hat{R} \cdot \vec{\nabla})]$, where $\hat{R} = \vec{R}/R$ and we set $\hbar = 1$. The Hamiltonian for a helical metal on a spherical surface is then given by

$$\mathcal{H}_0 = -\frac{\alpha}{R} \vec{L} \cdot \vec{\sigma} - \mu, \quad (2)$$

where \vec{L} is the orbital angular momentum. The single-particle Hamiltonian (2) can be solved easily. Define the total angular momentum $\vec{J} = \vec{L} + \vec{S}$. H_0 commutes with \vec{J} , the z component of \vec{J} (J_z), \vec{L} , and electron spin operator $\vec{S} = \vec{\sigma}/2$. The total angular momentum eigenvalue $j = 1/2$ if $l = 0$, and $j = l \pm 1/2$ if $l \neq 0$. The eigenenergy E_0 of Eq. (2) is given by

$$\begin{aligned} j = l + 1/2 : \quad E_+^0(l) &= -2\alpha \frac{l}{R} - \mu, \\ j = l - 1/2 : \quad E_-^0(l) &= 2\alpha \frac{l+1}{R} - \mu, \end{aligned} \quad (3)$$

and the two-component eigenstates in a compact form are

$$\begin{aligned} |j = l \pm 1/2, j_z, l, s = 1/2\rangle \\ = \alpha_{\pm} |l, j_z - 1/2\rangle \otimes |\uparrow\rangle + \beta_{\pm} |l, j_z + 1/2\rangle \otimes |\downarrow\rangle, \end{aligned} \quad (4)$$

where the Clebsch-Gordan (CG) coefficients are $\alpha_{\pm} = \pm\sqrt{(l \pm j_z + 1/2)/(2l + 1)} = \pm\beta_{\mp}$. There are $2j + 1$ degenerate states for a given eigenenergy, corresponding to different eigenvalues of J_z . Note that the states in $j = l + 1/2$ branch have negative energies without a lower energy bound, similar to the case in planar geometry. This will, however, not affect the basic physics near the Fermi energy, which we wish to address in this paper.

B. Proximity-induced superconducting state in a helical metal

We now consider the helical metal Hamiltonian with an additional pairing term describing proximity-induced superconductivity. We shall first consider a uniform pairing case that is free of vortices, described by

$$\mathcal{H}_{\Delta} = \Delta_0 \sigma_0 \otimes \tau_x, \quad (5)$$

where we use standard Nambu representation, for the field operator $\hat{\Psi}(\vec{r})$,

$$\hat{\Psi}(\mathbf{r}) = [\hat{c}_{\uparrow}(\mathbf{r}), \hat{c}_{\downarrow}(\mathbf{r}), \hat{c}_{\downarrow}^{\dagger}(\mathbf{r}), -\hat{c}_{\uparrow}^{\dagger}(\mathbf{r})]^T. \quad (6)$$

In Eq. (5), we have assumed the proximity induced superconducting order parameter Δ to be independent of the azimuthal angle θ and the polar angle ϕ . The total Hamiltonian then reads

$$\begin{aligned} \mathcal{H} &= \begin{pmatrix} \mathcal{H}_0 & \Delta_0 I \\ \Delta_0 I & -\sigma_y \mathcal{H}_0^* \sigma_y \end{pmatrix} \\ &= \left(-\frac{\alpha}{R} \vec{L} \cdot \vec{\sigma} - \mu \right) \otimes \tau_z + \Delta_0 \sigma_0 \otimes \tau_x, \end{aligned} \quad (7)$$

where $\vec{\tau}$ are Pauli matrices, with the two components representing particle-hole degrees of freedom, while $\vec{\sigma}$ is representing the spin degree of freedom, and σ_0 the identity matrix. Note that the total angular momentum $\vec{J} = \vec{L} + \vec{S}$ still commutes with \mathcal{H} in Eq. (7), the eigenenergies are given by

$$\begin{aligned} j = l + 1/2 : \quad E_{\pm}(l) &= \pm\sqrt{[E_{\pm}^0(l)]^2 + \Delta_0^2}, \\ j = l - 1/2 : \quad E_{\pm}(l) &= \pm\sqrt{[E_{\pm}^0(l)]^2 + \Delta_0^2}, \end{aligned} \quad (8)$$

where the corresponding four-component eigenfunction [see Eq. (4)] is $A|j = l \pm 1/2, j_z, l, s = 1/2\rangle \oplus B|j = l \pm 1/2, j_z, l, s = 1/2\rangle$ formally, in which the coefficients A and B satisfy the following equation:

$$A\Delta_0 = B[E_{\pm}^0 \pm \sqrt{(E_{\pm}^0)^2 + \Delta_0^2}], \quad (9)$$

where the normalization condition $A^2 + B^2 = 1$ gives $A = f/\sqrt{f^2 + \Delta_0^2}$ and $B = \Delta_0/\sqrt{f^2 + \Delta_0^2}$, with $f = E_{\pm}^0 + \sqrt{(E_{\pm}^0)^2 + \Delta_0^2}$ or $E_{\pm}^0 - \sqrt{(E_{\pm}^0)^2 + \Delta_0^2}$.

C. Vortex states in proximity-induced superconducting state of a helical metal

We proceed to consider the vortex case. The pairing Hamiltonian takes the form

$$\mathcal{H}_{\text{BdG}}(\Delta) = [\Delta(\theta)e^{i\phi}]\sigma_0. \quad (10)$$

In Eq. (10), the factor $e^{i\phi}$ describes a vortex with the winding number $n = 1$. Then we will use a numerical method to solve the vortex problem. The whole Bogoliubov-de Gennes Hamiltonian in the presence of the vortex consists of Eqs. (2) and (10),

$$\begin{aligned} \mathcal{H}_{\text{BdG}} &= \begin{pmatrix} \mathcal{H}_0 & \Delta(\theta)e^{i\phi} \\ \Delta(\theta)e^{-i\phi} & -\sigma_y \mathcal{H}_0^* \sigma_y \end{pmatrix} \\ &= \left(-\frac{\alpha}{R} \vec{L} \cdot \vec{\sigma} - \mu \right) \otimes \tau_z + \Delta(\theta)e^{i\phi} I \otimes \tau_x, \end{aligned} \quad (11)$$

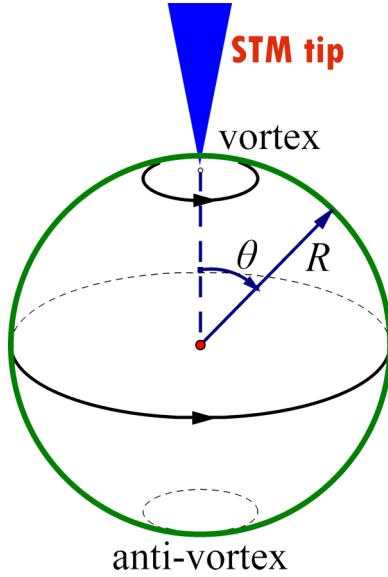


FIG. 1. Sphere geometry for the vortex problem. There exists a pair of vortex and antivortex. The vortex is located at the north pole and the antivortex is located at the south pole.

where we have neglected the bulk effect of TI, because only the surface physics is important according to Ref. [31]. We note that there is a vortex-antivortex pair, one of which (say, the vortex) is located at the north pole of the sphere and the other one (the antivortex) is at the south pole [32,33], see Fig. 1. In this paper, we assume the gap function $\Delta(\theta) = \Delta_0 \tanh[R \sin(\theta)/\xi_0]$, where ξ_0 characterizes the size of the vortex core.

In our model, we neglect the small Zeeman term and the vector potential. Neglecting the vector potential is a good approximation to describe the low magnetic field case, such as the experiment in Ref. [30], where the external magnetic field B is lower than 0.1 T. This approximation greatly simplifies the matter and is expected not to change our result qualitatively. Define the Bogoliubov quasiparticle operators as (using $r = R\theta$)

$$\hat{\gamma}^\dagger = \int d\mathbf{r} \left[\sum_{\sigma} u_{\sigma}(\mathbf{r}) \hat{c}_{\sigma}^{\dagger}(\mathbf{r}) + v_{\sigma}(\mathbf{r}) \hat{c}_{\sigma}(\mathbf{r}) \right]. \quad (12)$$

In passing, we remark that the necessary condition for the existence of the MZM is $\hat{\gamma}^\dagger = \pm \hat{\gamma}$. The spectra of the excitations of this system can be found by solving the eigenvalue problem in 2D coordinates $\{\theta, \phi\}$, similar to the calculations reported in Ref. [34]. Let $|\Phi_m\rangle$ be the four-component wave function of the field $\hat{\Psi}(\vec{r})$, and the eigenvalue problem is given by

$$\mathcal{H}_{\text{BdG}} |\Phi_m\rangle = E_m |\Phi_m\rangle, \quad (13)$$

with

$$|\Phi_m\rangle = (e^{im\phi} u_1, e^{i(m+1)\phi} u_2, e^{i(m-1)\phi} v_1, e^{im\phi} v_2)^T, \quad (14)$$

where m is the eigenvalue of K_z that will be defined in Eq. (15) below, and u_1, u_2, v_1, v_2 are real functions of θ and m , but are independent of ϕ . As we shall see below, there will be a pair of MZMs [11] in the channel $m = 0$. And the $m = \pm 1$ channel gives the first quasiparticle excitation [34,35]. Note

that the total angular momentum $J_z = L_z + \sigma_z/2$ does not commute with the Hamiltonian in Eq. (11), because of the winding phase factor $e^{i\phi}$ in the gap function. To solve the BdG Hamiltonian numerically, we observe that this Hamiltonian has a combined spin-orbit–pseudospin (pseudospin here refers to the particle-hole degree of freedom) rotational symmetry along the z axis. This symmetry can be expressed compactly by noting that the Hamiltonian in Eq. (11) commutes with a generalized total angular momentum including the pseudospin τ_z , so we have

$$K_z = L_z + \frac{1}{2}(\sigma_z - \tau_z) \Rightarrow [K_z, \mathcal{H}_{\text{BdG}}] = 0. \quad (15)$$

The BdG Hamiltonian can be decomposed into a block-diagonal form, with each block corresponding to a generalized total angular momentum m (quantum number of K_z), namely,

$$\mathcal{H} |\Phi_m\rangle = E |\Phi_m\rangle, \quad (16a)$$

$$K_z |\Phi_m\rangle = m |\Phi_m\rangle, \quad (16b)$$

where $|\Phi_m\rangle$ is given in Eq. (14). The four-component eigenfunction/basis in $|\Phi_m\rangle$ may be expressed in terms of the spherical harmonic functions:

$$e^{im\phi} u_1(m) = \sum_l a_l Y_l^m, \quad (17a)$$

$$e^{i(m+1)\phi} u_2(m+1) = \sum_l b_l Y_l^{m+1}, \quad (17b)$$

$$e^{i(m-1)\phi} v_1(m-1) = \sum_l c_l Y_l^{m-1}, \quad (17c)$$

$$e^{im\phi} v_2(m) = \sum_l d_l Y_l^m, \quad (17d)$$

with $Y_l^m(\theta, \phi) = P_l^m(\cos \theta) e^{im\phi} / \sqrt{2\pi}$, and P_l^m the associated Legendre polynomial. The above eigenstate problem can be solved numerically. The particle-hole symmetry $(-\sigma_y \tau_y K)$ is reflected as below. If we transform $m \rightarrow -m$, then we have $E_m \rightarrow -E_m$ and $\{u_1, u_2, v_1, v_2\} \rightarrow \{-v_2, v_1, u_2, -u_1\}$. Note that these wave functions are all real.

The system is invariant under rotation $\hat{O} = \hat{P} \sigma_z \otimes \tau_0$, which commutes with the Hamiltonian,

$$[\hat{O}, \mathcal{H}_{\text{BdG}}] = 0. \quad (18)$$

It means that the total Hamiltonian remains unchanged by transformation simultaneously both in real space $\hat{P} : \theta \rightarrow (\pi - \theta)$ and in spin subspace $\sigma_z : \sigma_x \rightarrow -\sigma_x, \sigma_y \rightarrow -\sigma_y$. This symmetry is important to analyze the twofold degeneracy of in-gap quasiparticle states in the large-radius limit. Assume $\mathcal{H}_{\text{BdG}} |\Phi_m^\pm\rangle = E_m^\pm |\Phi_m^\pm\rangle$ and $\hat{O} |\Phi_m^\pm\rangle = \pm |\Phi_m^\pm\rangle$, we can write down the in-gap quasiparticle wave functions in the form

$$|\Phi_m^\pm\rangle = e^{im\phi} [(u_1(\theta) \pm u_1(\pi - \theta)), e^{i\phi} [u_2(\theta) \mp u_2(\pi - \theta)], \\ \times e^{-i\phi} [v_1(\theta) \pm v_1(\pi - \theta)], [v_2(\theta) \mp v_2(\pi - \theta)]]^T. \quad (19)$$

To see the physical interpretation, we can define $|\Phi_m^N\rangle = (|\Phi_m^+\rangle + |\Phi_m^-\rangle) / \sqrt{2}$, which is localized at the north pole and vanishes at the south pole. Meanwhile, we also have $|\Phi_m^S\rangle = (|\Phi_m^+\rangle - |\Phi_m^-\rangle) / \sqrt{2}$, localized in the south pole. Therefore

the symmetry \hat{O} gives us the degenerated states ($|\Phi_m^{N/S}\rangle$) in the energy spectrum in the large-radius limit. However, this degeneracy will be lifted a little due to the hybridization between these two states in our numerical simulation, which is related to the finite size effect (finite radius R) and will be discussed in Sec. III B in details. Lastly, we also wish to emphasize that once all the eigenenergies and eigen-wave-functions are obtained, the Green's function, thereby the transport properties, can be calculated, as we will discuss in Sec. IV.

III. NUMERICAL RESULTS

In this section, we present the solutions of the BdG equations for the proximity-induced vortex states in a topological superconductor on a spherical surface and discuss the results in connection with recent experiments.

A. Energy spectra and wave functions

In our numerical calculations, we use parameters to approximately model the experiment in Ref. [23], in which the MZMs in $\text{Bi}_2\text{Se}_3/\text{NbSe}_2$ heterostructure has been detected. We set the parameters as follows, the coherence length $\xi_0 = 35$ nm is chosen as the length unit, the radius of the sphere $R = 50\xi_0$, the superconducting gap far away from the vortex core $\Delta_0 = 1$ meV, the chemical potential $\mu = 90$ meV and the spin-orbit coupling $\alpha = 30\xi_0$ meV nm. Note that the coherence length, the chemical potential, and the gap function are comparable to the extracted experiment data in Bi_2Se_3 of 35 nm, 100 meV, and 1 meV, respectively [23]. The Fermi velocity $v_F = \alpha\xi_0 = 1.05$ nm eV in our simulation is about 4 times larger than the experiment data of 0.27 nm eV [36,37]. The choice of a large spin-orbit coupling or a large Fermi velocity in our simulation is for the technique reasons in the calculations to avoid handling spherical harmonic functions of very large l , which turns to be quite challenging. The parameters used in our model calculations are close to those values used in the reported simulation in Ref. [30]. In our numerical calculations, we take a cutoff in the orbital angular momentum l around 200, which is sufficient to get the precise low-energy eigenvalues and the accurate corresponding spatial wave functions.

The energy spectra of the model Hamiltonian (11) are plotted in Fig. 2, where red circles represent several localized in-gap states in the vortex core. As a comparison, we plot the energy spectra of the vortex-free case in Fig. 13 in Appendix. The energy for MZM is about $E_0 = 10^{-4}$ meV due to the finite size effect.

The wave function for MZM with eigenenergy -10^{-4} meV is plotted in Fig. 3. We can see that around the north pole, $u_1 = v_2$ and $u_2 = v_1$, so that $\gamma = \gamma^\dagger$ (necessary condition for MZM). It is worth noting that the spin of MZM is fully polarized at the vortex core center and parallel to the magnetic field (spin up), say, $u_1 = v_2 \neq 0$ and $u_2 = v_1 = 0$ at $r = 0$. And, for this $|-E_0\rangle$ state, we notice that $u_1(\theta) = -u_1(\pi - \theta)$, $u_2(\theta) = u_2(\pi - \theta)$, $v_1 = -v_1(\pi - \theta)$, and $v_2(\theta) = v_2(\pi - \theta)$, leading to $\hat{O}|-E_0\rangle = -|-E_0\rangle$. Through the particle-hole symmetry, we can obtain the $|E_0\rangle$ state, which satisfies $\hat{O}|E_0\rangle = |E_0\rangle$. Therefore the tiny split

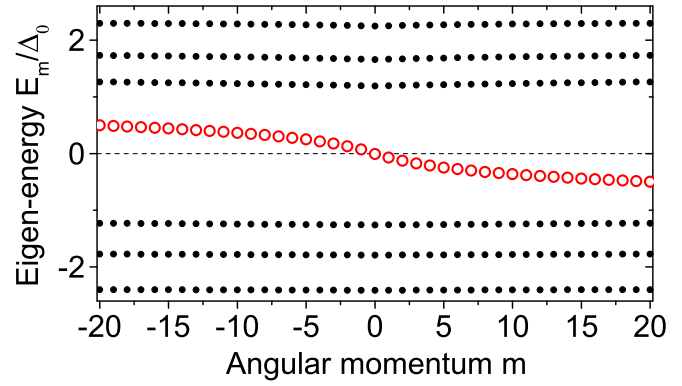


FIG. 2. Energy spectra for the vortex problem. E_m is plotted as a function of angular momentum m [quantum number of K_z in Eq. (15)]. Red hollow circular(\circ) represents localized in-gap bound states, and black solid circular(\bullet) represents bulk states. The energy discretization for bulk states is due to finite size effect. Here we choose parameters as $\Delta_0 = 1$ meV, $\xi_0 = 35$ nm, $R = 50\xi_0$, $\alpha = 30$ meV, and $\mu = 90$ meV.

of these two almost degenerate states around $E = 0$ gives particle-hole symmetry.

Fig. 4 shows the wave function of the first excited state E_1^- (quasihole). It is clear that the spin is still fully polarized at the vortex core center but opposite to the magnetic field (spin down). Note that there is only one nonzero component in the wave function at the vortex core center, namely, $v_1(r = 0) \neq 0$ and $u_1(r = 0) = u_2(r = 0) = v_2(r = 0) = 0$. The energy of the first excited state in Fig. 4 is found to be $E_1 \approx 0.05$ meV.

The wave functions of the other high angular momentum with $m = 2, 3, 4, 5$ are shown in Fig. 5. It is interesting to note that the spherical harmonic function $Y_l^m(\theta, \phi) = 0$ at $\theta = 0$ and $\theta = \pi$ for all angular momenta m except the $m = 0$ channel. Therefore all the eigen-wave-functions $|\Phi_m\rangle$ with $|m| > 1$ in Eq. (17) for the in-gap states in the vortex core have zero amplitudes at $\theta = 0$ and $\theta = \pi$. This property will greatly

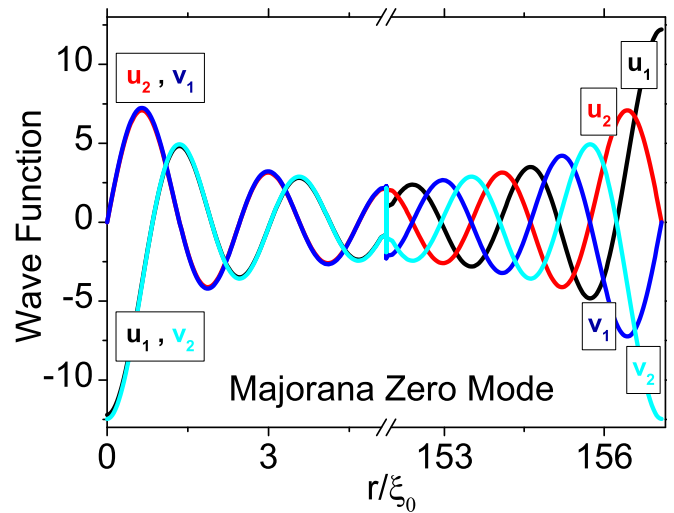


FIG. 3. Wave function for Majorana zero mode $E_0^- \approx -10^{-4}$ meV, where $u_1(\theta) = -u_1(\pi - \theta)$, $u_2(\theta) = u_2(\pi - \theta)$, $v_1(\theta) = -v_1(\pi - \theta)$, and $v_2(\theta) = v_2(\pi - \theta)$.

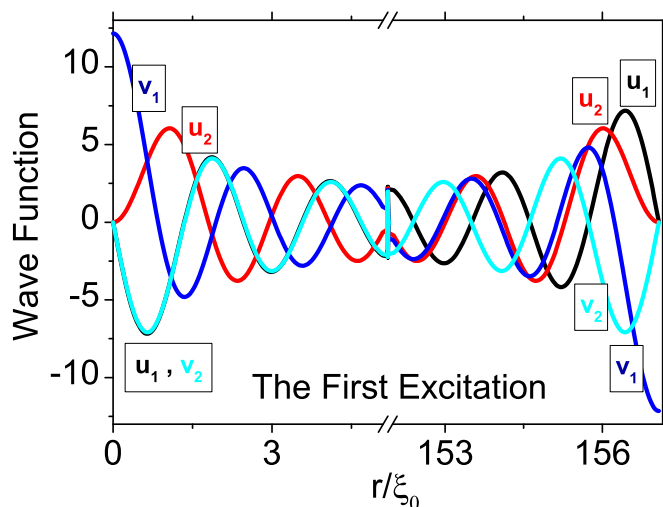


FIG. 4. Wave function for the first excited state $E_1^- \approx -0.05$ meV, where $u_1(\theta) = -u_1(\pi - \theta)$, $u_2(\theta) = u_2(\pi - \theta)$, $v_1(\theta) = -v_1(\pi - \theta)$, and $v_2(\theta) = v_2(\pi - \theta)$.

simplify the calculations of the local tunneling conductance at the vortex center discussed in Sec. III C. The energy for the second excited state is $E_2 \approx 0.1$ meV. Finally, we would like to point out that the low lying energy separation of the quasiparticle states in our present calculations appears to be larger than the estimated one in a vortex core, which is given by $\Delta_0^2/\mu \approx 0.01$ meV in Ref. [23], which could be due to the discrete energy spectra in the free electron system of the model.

TABLE I. Energy for the first excited in-gap quasiparticle state E_1^\pm for different radii. Parameters are $\mu = 84$ meV, $\Delta_0 = 1$ meV, and $\alpha = 25$ meV.

| | $R = 50\xi_0$ | $R = 40\xi_0$ | $R = 30\xi_0$ |
|---------|---------------|---------------|---------------|
| E_1^- | 0.065047 | 0.053 | 0.038 |
| E_1^+ | 0.065062 | 0.078 | 0.093 |

B. Two-vortex hybridization (finite size effect)

In this section, we shall study the two-vortex-hybridization problem through the finite size effect in our model. For experiments, increasing the external magnetic field will shorten the distance between the two nearest-neighbor vortices on the Abrikosov lattice. So that the two-vortex-hybridization effect will be significant in the presence of a higher magnetic field. Theoretically, we have a pair of vortex and antivortex located at the north and south poles on the sphere, respectively. Decreasing the sphere radius while keeping the coherence length unchanged will give rise to a stronger hybridization between the vortex and the antivortex and lift the twofold degeneracy and vice versa. Therefore the two-vortex problem can be reflected as a finite size effect in our model.

To study the finite size effect, let us take an example by using a set of parameters: $\mu = 84$ meV, $\Delta_0 = 1$ meV, and $\alpha = 25$ meV. The energies of the first excited in-gap quasiparticle E_1^\pm for different radii R are summarized in Table I. For a sufficient large radius $R = 50\xi_0$, the two states shown in Eq. (19) are almost degenerate. However, for a smaller radius $R = 30\xi_0$, the degeneracy of these two states will be totally lifted.

We now discuss the finite size effect on the two MZM states with tiny hybridization. The parameters mentioned in

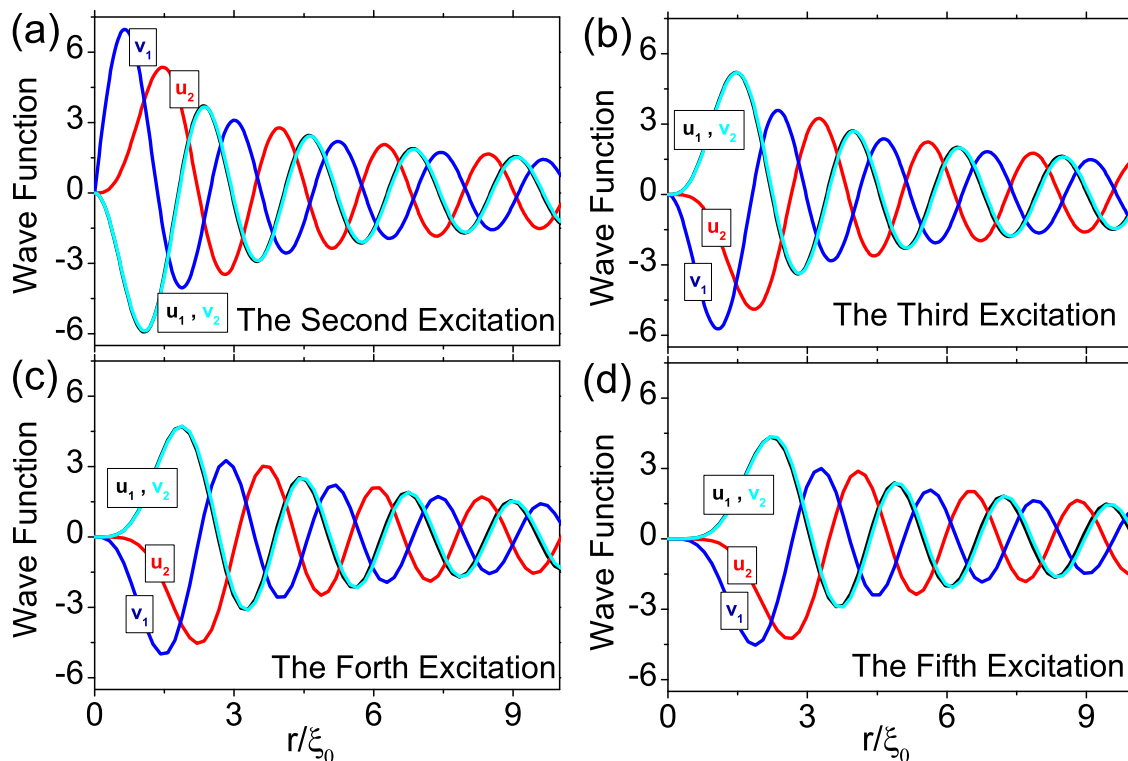


FIG. 5. Wave function for the second (a), third (b), fourth (c), and fifth (d) excited states.

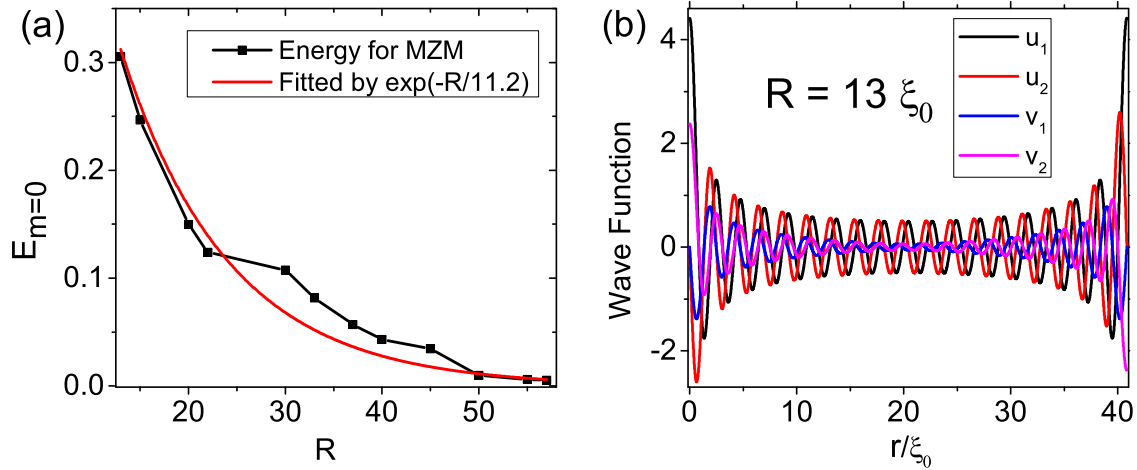


FIG. 6. Two-vortex hybridization effect. (a) The energy of the $m = 0$ state (MZM) for different sphere radii R . (b) The wave function of MZM for a small size $R = 13\xi_0$.

Sec. III A have been used to generate MZMs, and the radius of the sphere is $R = 50\xi_0$, which is large enough to separate the MZM in a north pole and in a south pole part. In Fig. 3, we show the wave function around both north and south poles as a function of $r = R\theta$, which will decay to zero before reaching the equator of the sphere (not shown in the figure). Recall that we use a vortex-antivortex pair on a sphere, i.e., $\Delta(\theta) = \Delta_0 \tanh(R \sin \theta / \xi_0)$. Now, if we change the distance between the north (vortex) and south poles (antivortex) by decreasing the radius R of the sphere, then we find in our calculation that the energy for the MZM, E_0 , increases drastically to a finite energy (order of superconductor gap) [34,38,39], shown in Fig. 6(a).

From Fig. 6(b), we can see that the wave function of the MZM in the north pole is hybridized with the MZM in the south pole. As a result, the condition for MZM $\gamma = \gamma^\dagger$ is not satisfied in the small radius case (here we set $R = 13\xi_0$), and the two MZMs meet each other and evolve into two non-MZM states (say, complex quasiparticles) with a finite subenergy gap. For example, the finite energy E_0 is about $\pm 0.3\Delta_0$ for the $R = 13\xi_0$ case. In this case, the MZM is not localized but looks like a bulk state as shown in Fig. 6(b). The loss of the self-conjugate condition, together with the loss of the localization condition, will give an extremely different Andreev reflection result, which will be discussed in Sec. IV B.

As for the experiment data in Ref. [23], it is found that a small external magnetic field (up to 0.18 T) perpendicular to the surface will make the Abrikosov vortices closer and closer, leading to a weaker and weaker zero-bias peak in STM/STS experiments. This can be easily understood from our model calculation, because the hybridization of MZM's wave functions between two adjacent vortices will open a finite gap, see Fig. 6(a), where the black line is from our numerical calculation, and the red line is fitted by a function $\exp(-R/11.2)$.

C. Local density of states and normal conductance

To analyze the experimental data from spin-resolved STM, we should consider both normal conductance and Andreev reflection [40–43]. In this section, we shall calculate the local

density of states (LDOS) and then estimate the normal conductance. As we know, the normal conductance is proportional to the local density of states $\mathcal{N}(E, r)$,

$$\sigma_n(E, r) \equiv dI/dV(E, r) = \bar{\alpha} \mathcal{N}(E, r), \quad (20)$$

where $\bar{\alpha}$ is assumed to be a constant. Under this approximation, we may estimate the normal conductance as follows:

$$\sigma_n(E < \Delta_0, r) = \sigma_n(\bar{E} \gg \Delta_0, r) \times \frac{\mathcal{N}(E < \Delta_0, r)}{\mathcal{N}(\bar{E} \gg \Delta_0, r)}. \quad (21)$$

Here, $\sigma_n(\bar{E} \gg \Delta_0)$ is the single-particle tunneling conductance for the normal state. Since the superconducting gap is induced by the proximity effect (Δ_0 is only 1 meV), we may treat the normal state as helical metal when $\bar{E} \gg \Delta_0$ and $\epsilon(\mathbf{k}) = \pm\sqrt{(\alpha|\mathbf{k}| \pm \mu)^2 + \Delta_0^2} \approx \pm(\alpha|\mathbf{k}| \pm \mu)$ as in Ref. [8]. Then we can set up a junction consisting of a 1D normal lead/1D helical metal/1D helical metal lead [see Fig. 7(a)] to calculate the single-particle tunneling conductance for the helical metal. By using the recursive Green's function

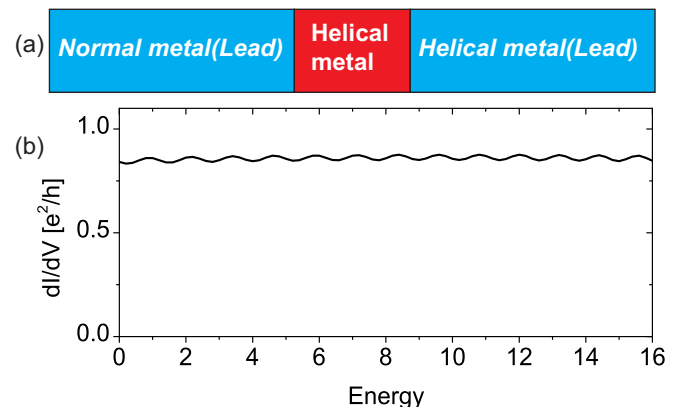


FIG. 7. (a) The normal metal (lead)/helical metal/helical metal (lead) junction used to estimate the normal conductance in STM/STS experiments. (b) Calculated normal conductance, $\sigma_n(\bar{E} \gg \Delta_0) \approx 0.88 e^2/h$, where we choose the hopping integral in the normal lead $t' = 24$ and the coupling between the helical metal and left and right leads as $t_L = t'$ and $t_R = 0.85t'$.

method and the Landauer-Büttiker formula [44], we obtain $\sigma_n(\bar{E} \gg \Delta_0) \approx 0.88 e^2/h$ as shown in Fig. 7(b). Therefore the normal conductance is given by

$$\sigma_n(E < \Delta_0, r) = \frac{\mathcal{N}(E < \Delta_0, r)}{\mathcal{N}(\bar{E} \gg \Delta_0, r)} \times 0.88 e^2/h. \quad (22)$$

Thus the problem is reduced to the calculation of the spin-polarized LDOS for quasiparticle excitations [45], which is given by the electron wave functions

$$\mathcal{N}(E, r) = \mathcal{N}_\uparrow(E, r) + \mathcal{N}_\downarrow(E, r), \quad (23)$$

$$\mathcal{N}_\uparrow(E, r) = \sum_{E_m} [|u_1|^2 \delta(E - E_m) + |v_2|^2 \delta(E + E_m)], \quad (24)$$

$$\mathcal{N}_\downarrow(E, r) = \sum_{E_m} [|u_2|^2 \delta(E - E_m) + |v_1|^2 \delta(E + E_m)], \quad (25)$$

where $\delta(E - E_m)$ will be replaced by a smearing Gaussian function,

$$\delta(E - E_m) = \exp[-(E - E_m)^2/\eta^2]/(\sqrt{\pi}\eta), \quad (26)$$

where the smearing factor η can be chosen smaller than the excitation gap $\Delta E = E_1 - E_0$ in a vortex core, as well as larger than ΔE , which is the case in STM/STS experiments.

It is well known that the spectra of LDOS in a vortex are discretized inside the gap and consist of several isolated peaks [46,47]. Especially, there are only two bound-state peaks contributing to the spectra of LDOS at the vortex core center $r = 0$. Since LDOS is proportional to the amplitude square of the wave function, and we have proved in Sec. III A that $\Phi_m(\theta = 0) = \Phi_m(\theta = \pi) = 0$ for $|m| > 1$ (also see Figs. 3 and 4), only the MZM (E_0) and the first excited state (E_1) will contribute to the bound-state peaks.

In Fig. 8, we plot the LDOS at $r = 0$ for three values of the smearing factor η in Eq. (26). For $\eta \ll E_1$, the LDOS for the spin up (\mathcal{N}_\uparrow , MZM contribution) and for the spin down (\mathcal{N}_\downarrow , the first excited state) are well separated in energy as shown in Fig. 8(a). This also indicates the particle-hole asymmetry in vortex bound states as discussed in Refs. [45,47–49]. For $\eta \sim E_1$, $\mathcal{N}_\uparrow(E)$ and $\mathcal{N}_\downarrow(E)$ overlap but are still distinguishable as plotted in Fig. 8(b). For $\eta \gg E_1$, $\mathcal{N}_\uparrow(E)$ and $\mathcal{N}_\downarrow(E)$ become essentially the same. Note that η is a measure of the energy resolution in the STM experiment, which is presently poor to distinguish E_1 from the zero mode. We believe that Fig. 8(c) corresponds to the experimental situation in Ref. [30]. It is a

very important conclusion in this paper. We also note that a similar result was reported in Ref. [45].

IV. ANDREEV REFLECTION

In this section, we present the method and results for the calculation of Andreev reflection (AR) based on the solution of BdG equations, and explain recent experiments in Ref. [30]. We consider the tiny STM tip as a 1D metallic lead and “touch” the vortex core as a single point contact. We argue that this should be a good approximation in the high-barrier limit. The s -wave superconducting gap will induce effective triplet pairing correlations in the bulk spectrum for a system with strong spin-orbit coupling [13,50]. However, it will not affect our discussions on spin-selective Andreev reflection (SSAR) for MZM, because we only focus on the center of the vortex core, where the superconducting gap is zero.

An MZM [10,51] will contribute to the measurement of dI/dV for a 1D nanowire system via Andreev reflection [52]. Moreover, He *et al.* figured out that spin-selective Andreev reflection (SSAR) can be used to reveal the spin degree of freedom for an MZM, and they demonstrated it in a 1D nanowire system [25]. As for the measurement of the SSAR (SESAR) effect of a 1D nanowire system, where there is no direct contact from the lead to the s -wave superconductor, it will be possible for a system with a larger g factor so that a smaller magnetic field will be required to drive the 1D nanowire system into a topological phase satisfying $V_z^2 > \Delta_0^2 + \mu^2$. Recently, the out-of-plane g factor was found to be about 52 for an InSb nanowire, reported in Ref. [53]. Besides, it may also be possible to use the SSAR effect to distinguish the MZM from the normal Yu-Shiba-Rusinov in-gap states in the ferromagnetic atomic chains on a s -wave superconductor [22]. In this paper, we theoretically generalize He *et al.*'s theory to the TI/SC heterostructure modeled in Eq. (11), and find a similar SSAR inside the vortex core, which provides strong evidence to the existence of MZMs.

A. Transport method for a normal metal/superconductor junction

To study the SSAR contribution to the total conductance measured in spin-polarized STM/STS experiments, we utilize the setup sketched in Figs. 1 and 9. Since the STM tip size in STM/STS experiments is about 0.01 nm, which is much smaller than the vortex size $\xi_0 = 35$ nm, we can treat the STM

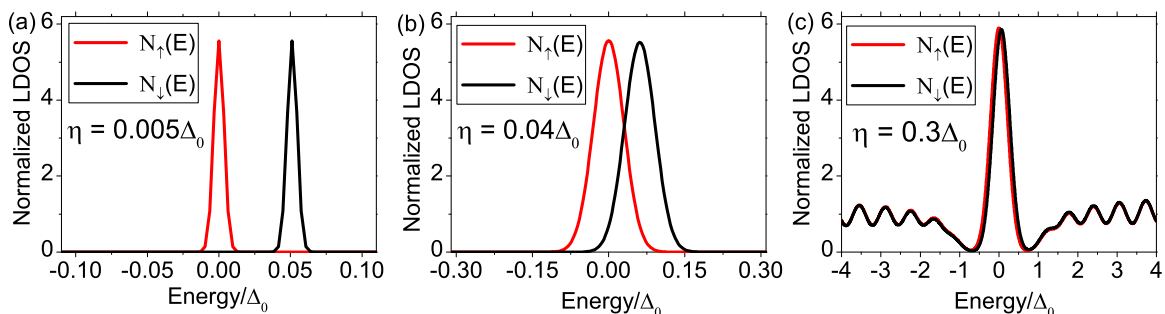


FIG. 8. Local density of states. (a) The smearing factor defined in Eq. (26) $\eta = 0.005\Delta_0$. (b) $\eta = 0.04\Delta_0 \sim E_1$, comparable to the first excited state energy. (c) $\eta = 0.3\Delta_0 \approx 6E_1$. The LDOS for spin-up $\mathcal{N}_\uparrow(E)$ and spin-down $\mathcal{N}_\downarrow(E)$ coincide to each other.

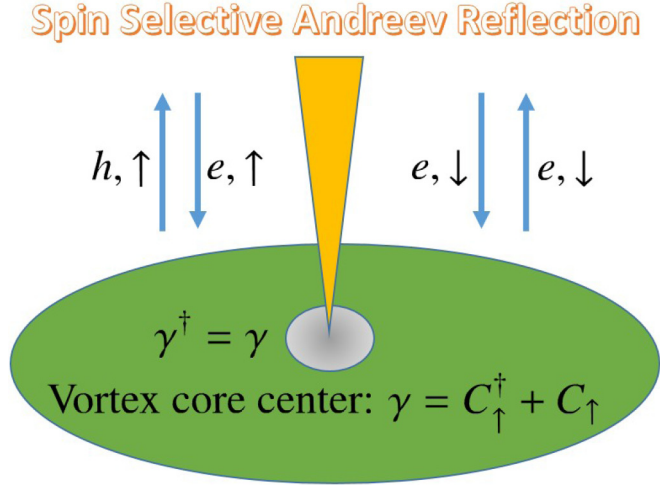


FIG. 9. Illustration of spin-selective Andreev reflection. An incoming spin-down electron will be reflected as a spin-down electron because of the mismatch of the spins of the incoming electron and the MZM.

tip as a normal lead and the contact between the STM tip and TI/SC as a point contact. The normal lead can be described by the following Hamiltonian:

$$\mathcal{H}_L = \sum_{i < 0, \sigma} \{-t' \hat{c}_{Li\sigma}^\dagger \hat{c}_{Li+1\sigma} + \text{H.c.}\} + \{(2t' - \mu') \hat{c}_{Li\sigma}^\dagger \hat{c}_{Li\sigma} + \hat{c}_{Li\alpha}^\dagger [\vec{V} \cdot \vec{\sigma}]_{\alpha, \beta} \hat{c}_{Li\beta}\}. \quad (27)$$

The coupling between the normal lead and TI/SC (the contact point locates inside the vortex core) is given by

$$\mathcal{H}_t = \sum_{\sigma} \{t_c \hat{c}_{L0\sigma}^\dagger \hat{c}_{S1\sigma} + \text{H.c.}\}. \quad (28)$$

To proceed, we shall demonstrate the SSAR induced by MZMs in the high-barrier limit and choose the parameters as follows: $|\vec{V}| = 10\Delta_0$, $t' = 25\Delta_0$, $\mu' = 0$, and $t_c = 0.008\Delta_0$. Note that the coupling strength t_c only affects the width of the zero-bias peak of an MZM, which is of the Lorentz shape [25], $dI/dV \sim E^2/(E^2 + \tilde{\Gamma}^2)$, where $\tilde{\Gamma} \sim t_c$. Other parameters in the TI/SC heterostructure are chosen the same as those in Sec. III A.

With the help of the solution to Eq. (13), we are able to calculate the retarded Green's function for the single-particle system,

$$G_0^R(E, \vec{r}, \vec{r}') = \sum_m \sum_n \frac{|\Phi_m^n(\vec{r})\rangle \langle \Phi_m^n(\vec{r}')|}{E - E_m^n + i\delta}, \quad (29)$$

where m is the angular momentum [quantum number of K_z in Eq. (15)], n is an additional quantum number labeling the eigenstates, δ is a positive infinitesimal and set as 10^{-5} meV in our calculation, and G_0^R is a 4×4 matrix.

For the point contact problem, we need to evaluate the local Green's function $G^{\text{tot}}(E, \vec{r}, \vec{r})$ in the coupled system. Considering the δ function interaction between the normal lead and the 2D TI/SC heterostructure, we can write $G^{\text{tot}}(E, \vec{r}, \vec{r})$ in terms of $G_0^R(E, \vec{r}, \vec{r})$ and self-energy $\Sigma(E, \vec{r})$ through the

Dyson equation [44,54],

$$G^{\text{tot}}(E, \vec{r}, \vec{r}) = \frac{1}{(G_0^R(E, \vec{r}, \vec{r}))^{-1} - \Sigma(E, \vec{r})}, \quad (30)$$

or its iterative form

$$G^{\text{tot}}(E, \vec{r}, \vec{r}) = G_0^R(E, \vec{r}, \vec{r}) + \Sigma(E, \vec{r}) G^{\text{tot}}(E, \vec{r}, \vec{r}). \quad (31)$$

After that, the S matrix for the junction can be calculated by the Fisher-Lee formula [55–57],

$$\tilde{S} = -I + i\Gamma^{1/2} \times G^{\text{tot}} \times \Gamma^{1/2}, \quad (32)$$

where the broadening function Γ is defined as $\Gamma = i(\Sigma - \Sigma^\dagger)$, which is a 4×4 matrix too. We can read out the 2×2 reflection matrices \tilde{r}_{ee} and \tilde{r}_{he} from the S matrix,

$$\tilde{S} = \begin{pmatrix} \tilde{r}_{ee} & \tilde{r}_{eh} \\ \tilde{r}_{he} & \tilde{r}_{hh} \end{pmatrix}, \quad (33)$$

where $\tilde{r}_{ee}^{\sigma, \sigma'}$ means that a spin- σ' electron comes in and a spin- σ electron goes out. Thus we can calculate the differential conductance coming from Andreev reflection dI/dV using the Landauer-Büttiker formula [44],

$$\sigma_A(E, \vec{r}) \equiv dI/dV(E, \vec{r}) = \text{Tr}[\tilde{r}_{he}^\dagger \tilde{r}_{he}] \times 2e^2/h. \quad (34)$$

B. Spin-selective Andreev reflection

In this section, we will discuss the SSAR effect and focus on the vortex core center $r = 0$, where the MZM spin is parallel to the magnetic field (spin up) by symmetry. The case of $r = 0$ also means that we only need to keep the $m = 0$ channel in Eq. (29), which will greatly simplify our dI/dV calculations. Because the normal vortex states of $m = \pm 1$ channels have only a single nonvanishing component, separately, they will not contribute to the anomalous part of the Green's function in Eq. (29). Also, note that all vortex states with high angular momentum channels with $|m| \geq 1$ vanish at the vortex core.

As pointed out by He *et al.* [25], an incoming spin-up electron will be reflected as a spin-up hole, while an incoming spin-down electron will be reflected as a spin-down electron because of the mismatch of the spins of the incoming electron and the MZM. This phenomenon is called spin-selective Andreev reflection (SSAR) [25,30], as illustrated in Fig. 9. Note that the superconducting gap vanishes at the vortex core center $r = 0$, therefore the Andreev reflection is via the MZM only.

We would like to emphasize that both MZM (large radius $R \sim 50\xi_0$) and non-MZM states (small radius $R \sim 13\xi_0$) for the $m = 0$ channel have nonzero u_1 and v_2 which, in principle, will lead to an SSAR signal at the vortex core center. And the MZM case will give a zero-bias peak, while the non-MZM case will give two peaks at finite energy $\pm E_0 \sim 0.3\Delta_0$. To examine this point, we shall study SSAR in our model with two different sphere radius sizes, $R = 50\xi_0$ and $R = 13\xi_0$. As discussed in Sec. III B, (i) when $R = 50\xi_0$, there exists a single MZM ($\gamma = \gamma^\dagger$) inside each vortex and antivortex core, which is well separated from each other; (ii) when $R = 13\xi_0$, two MZMs will hybridize with each other strongly, resulting in non-MZM states ($\gamma \neq \gamma^\dagger$) with extended spatial wave functions.

Numerical results for the AR conductance dI/dV are plotted in Fig. 10. For the large radius $R = 50\xi_0$ with a well

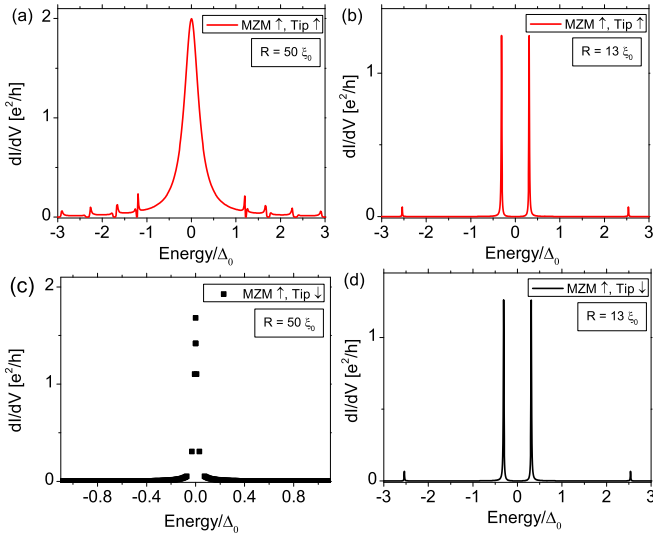


FIG. 10. Calculated AR conductance dI/dV at vortex core center $r = 0$. (a) $R = 50\xi_0$, the incoming electron spin polarization is parallel to local MZM spin. (b) $R = 13\xi_0$ the incoming electron spin polarization is parallel to local non-MZM spin. (c) $R = 50\xi_0$, the incoming electron spin polarization is antiparallel to local MZM spin. (d) $R = 13\xi_0$, the incoming electron spin polarization is antiparallel to the local non-MZM spin.

localized MZM, when the incoming electron spin polarization is parallel to the MZM spin at the vortex core center, the AR conductance dI/dV exhibits a zero-bias peak with a quantized conductance $2e^2/h$ and significant weight in the spectra, as shown in Fig. 10(a). However, for the small radius $R = 13\xi_0$ with two strongly hybridized MZMs, dI/dV only has two sharp peaks at finite energy with almost vanishing weight, as plotted in Fig. 10(b). However, if we increase the coupling $t_c \sim 0.04\Delta_0$ for the $R \sim 13\xi_0$ case, the width of these two peaks will be increased but the height is still lower than $2e^2/h$ (not shown). Indeed, similar sharp peaks also appear in the ordinary Andreev reflection in s -wave superconductors at the superconducting gap edge in the high-barrier limit, see Appendix for details. On the contrary, when the incoming electron spin polarization is antiparallel to the MZM spin at the vortex core center, the signal of the AR conductance is completely suppressed for both the large and the small radius, as shown in Figs. 10(c) and 10(d). The very tiny width of the peak in the calculations of the AR conductance for the antiparallel spin case does not increase as the contact coupling t_c increases. Such a peak for the antiparallel spin case was also observed in the calculation of He *et al.* [25] for AR conductance in nanowire with Majorana particles at the ends, and due to the resonance. Because of the finite energy resolution ΔE in the STM, what the STM measured is local conductance at an energy within an energy interval of ΔE , which is larger than the width of the peak in Fig. 10(a), hence the weight of the conductance spectra of the peak is very small or even vanishingly small. Therefore one can conclude that the Andreev reflection is spin-selective at the vortex core center in the presence of a localized MZM. The comparison of Fig. 10(b) for the small radius of the sphere with Fig. 10(a) for the large radius illustrates that a large hybridization between the two

MZMs (vortex and antivortex at the two poles) suppresses the AR conductance.

It is noted that the results in Fig. 10 also explain the experimental fact that all the zero-bias peaks in dI/dV of AR will disappear when the external magnetic field exceeds a small threshold value. The reason is the following. Increasing the external magnetic field will shorten the distance between two neighboring vortices on the Abrikosov lattice. Then an MZM inside a vortex core will hybridize with another one in the neighboring vortex core, leading to non-MZM states with a finite subenergy gap instead of MZMs. Such a non-MZM state will contribute an almost vanishing AR signal with a high-barrier limit $t_c \sim 0.008\Delta_0$ between the STM tip and the surface of the TI.

C. Total differential conductance in spin polarized STM/STS experiments

The total conductance in spin polarized STM/STS experiments can be evaluated by adding the normal component $\sigma_n(E, r)$ in Eq. (22) to the AR component $\sigma_A(E, r)$ in Eq. (34),

$$\sigma_{\text{tot}}(E, r) = \sigma_n(E, r) + \sigma_A(E, r). \quad (35)$$

Although the STM tip can be located in arbitrary r in STM/STS experiments, the SSAR effect will be suppressed and then vanish as r increases, when the differential conductance dI/dV is no longer spin dependent. So that let us focus on $r = 0$ at first, and then discuss how $r > 0$ will change the results.

The numerical results at $r = 0$ are shown and compared with experimental data in Fig. 11. In our calculations, we choose two different energy smearing factors defined in (26), $\eta = 0.04\Delta_0$ and $0.3\Delta_0$. The former is chosen as close to the first in-gap excited energy E_1 , while the latter is close to energy resolution in STM/STS experiments [30]. The calculated total conductance dI/dV for $\eta = 0.04\Delta_0$ and $0.3\Delta_0$ is plotted in Figs. 11(a) and 11(b) respectively, and the experimental result [30] is plotted in Fig. 11(c) for comparison.

For $\eta = 0.04\Delta_0 \sim E_1$, the total conductance dI/dV exhibits two distinguishable peaks for different spin polarization, see Fig. 11(a). When the STM tip spin polarization is parallel to the MZM spin (is parallel to external magnetic field at $r = 0$), which is denoted as “MZM \uparrow , Tip \uparrow ”, there is a zero-bias peak. When the spin polarization of the tip is antiparallel to the MZM spin, denoted as “MZM \uparrow , Tip \downarrow ”, there is a peak around E_1 . Hereafter, we shall denote the height of these two peaks as $dI/dV|_{\uparrow}$ and $dI/dV|_{\downarrow}$, respectively. The separation of these two peaks in energy is due to the LDOS, see Fig. 8, which contributes to the normal conductance σ_n .

For $\eta = 0.4\Delta_0 \gg E_1$, which is close to the experimental situation, there exist two zero-bias peaks in dI/dV as shown in Fig. 11(b), with height $dI/dV|_{\uparrow}$ and $dI/dV|_{\downarrow}$. Since LDOS is almost spin independent in this case, $\mathcal{N}_{\uparrow} = \mathcal{N}_{\downarrow}$, therefore, the normal conductance is spin independent too and the difference between $dI/dV|_{\uparrow}$ and $dI/dV|_{\downarrow}$ comes from SSAR entirely. The spin polarization of the tunneling conductance is estimated as

$$P = \frac{dI/dV|_{\uparrow} - dI/dV|_{\downarrow}}{dI/dV|_{\uparrow} + dI/dV|_{\downarrow}} \sim 16\%, \quad (36)$$

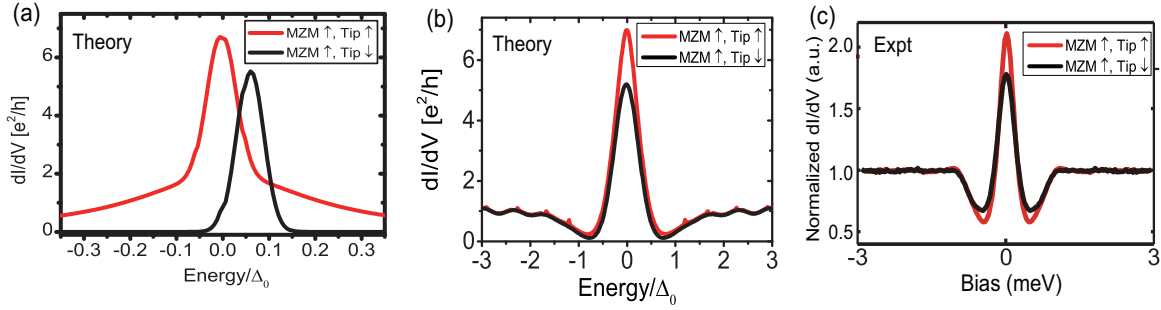


FIG. 11. (a) Calculated total conductance with $\eta = 0.04\Delta_0$. (b) Calculated total conductance with $\eta = 0.3\Delta_0$. (c) Experiment data from Ref. [30].

which is about 2.3 times of the experimental value 7% [30], see Fig. 11(c) for details. The deviation from the experimental value may be due to disorder effect, which has not been yet considered in this paper.

Now, let us discuss the situation when $r > 0$. Due to the spin-orbit coupling, the spin of MZM is not a good quantum number and will vary spatially. On the other hand, the amplitude of the MZM wave function, $|u_1|^2 + |u_2|^2$, will decay as r increases. The angle between the local spin direction of the MZM and the external magnetic field θ_M is plotted as a function of r as well as the amplitude $|u_1|^2 + |u_2|^2$ in Fig. 12. When the STM tip moves away from the vortex core center, two reasons will reduce the SSAR signal. Firstly, the amplitude of MZM wave function becomes smaller and smaller. Secondly, the mismatch between the STM tip spin polarization and the local spin of MZM will reduce the AR conductance via MZM. This explains the experimental observation that the spin dependence of dI/dV becomes too weak to detect at about $r = 0.3\xi_0$ [30].

V. CONCLUSIONS

In this paper, we use the proposal by Fu and Kane [8] to generate the MZM in the vortex core on the interface between TI and SC. Then, we take the parameters derived from the

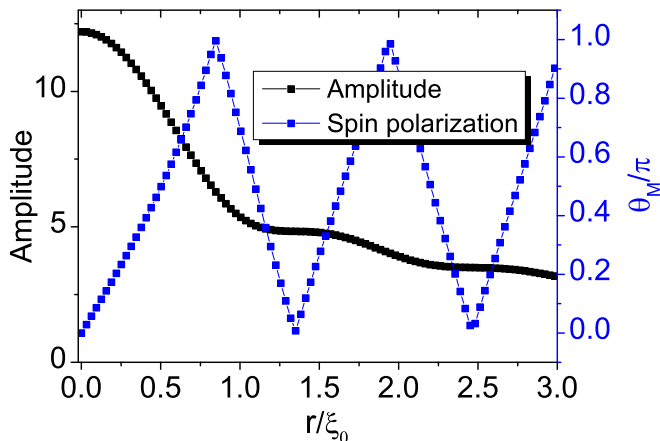


FIG. 12. The angle between the local MZM spin and external magnetic field θ_M and the amplitude of MZM wave function $\sqrt{|u_1(r)|^2 + |u_2(r)|^2}$. $\theta_M = 0$ is for parallel and $\theta_M = \pi$ is for antiparallel.

experiment to solve the BdG equation in Eq. (11). Based on the results for both larger radius and smaller radius, we simulate the distance between the vortex in the north pole and the vortex in the south pole, so that we can discuss the two-vortices problem (finite size effect). It may be related to the experiment, in which the external magnetic field will make the vortices closer and closer so that the ZBP will disappear. We think it is because of the hybridization of MZMs' wave functions in nearby vortices, which will lead to a finite subenergy gap. In addition, we calculate the LDOS for a small smearing factor and larger smearing. The asymmetry of LDOS has not been seen in experiment so far, because the STM energy resolution (0.1 meV) is larger than the minigap (0.05 meV). Finally, we use the Green function's approach to calculate the S matrix for an N/S junction by Fish-Lee-Landauer-Büttiker formula, and we find a similar SSAR effect in our model calculation. Finally, we also estimate that the total conductance dI/dV in our calculation is qualitatively consistent with the experiment [30].

Furthermore, we wish to point out that the estimation for a normal conductance here is considered in an approximated way. A precise calculation may change our results a little, but the main physics should remain as we discussed in this paper, due to the spin property of MZMs.

ACKNOWLEDGMENTS

We acknowledge helpful discussions with Chih-Chieh Chen, Chui-Zhen Chen, Fei Ye, Jin-Hua Gao, Wei-Qiang Chen, and K. T. Law. Especially, we benefit a lot from detailed communications with Jin-Feng Jia, Haohua Sun, and James Jun He. This work is supported in part by National Basic Research Program of China (Grant No. 2014CB921201/2014CB921203), National Key R&D Program of the MOST of China (Grant No. 2016YFA0300202), NSFC (Grant No. 11374256/11274269), and the Fundamental Research Funds for the Central Universities in China. F.-C.Z was also supported by the Hong Kong's University Grant Council via Grant No. AoE/P-04/08.

APPENDIX: REPRODUCE BTK THEORY

In this Appendix, we shall discuss the vortex-free case in details. In this case, the superconducting gap is a constant, i.e., $\Delta(\theta, \phi) = \Delta_0$. Although the analytical solution to Hamiltonian (7) has been derived in Eq. (8), we would

like to use the numerical method, discussed in the main text in Sec. II, to solve this problem once more and reproduce the results of BTK theory for a double check. For a conventional s -wave superconductor, the kinetic term may involve $\eta L^2/R^2$ and drop out the linear term. The Hamiltonian

$$\mathcal{H}_{\text{BdG}} = \begin{pmatrix} \frac{\eta}{R^2}L^2 - \mu - \frac{\alpha}{R}L_z & -\frac{\alpha}{R}L_- & \Delta_0 & 0 \\ -\frac{\alpha}{R}L_+ & \frac{\eta}{R^2}L^2 - \mu + \frac{\alpha}{R}L_z & 0 & \Delta_0 \\ \Delta_0 & 0 & -(\frac{\eta}{R^2}L^2 - \mu) + \frac{\alpha}{R}L_z & \frac{\alpha}{R}L_- \\ 0 & \Delta_0 & \frac{\alpha}{R}L_+ & -(\frac{\eta}{R^2}L^2 - \mu) - \frac{\alpha}{R}L_z \end{pmatrix}. \quad (\text{A2})$$

Since J_z is still a good quantum number in this situation, the same technique to solve the BdG equation in the main text is still valid here, expect that the basis in Eqs. (16a) and (16b) will change. Now the secular equations become

$$\mathcal{H} \begin{pmatrix} e^{im\phi} u_1 \\ e^{i(m+1)\phi} u_2 \\ e^{im\phi} v_1 \\ e^{i(m+1)\phi} v_2 \end{pmatrix} = E \begin{pmatrix} e^{im\phi} u_1 \\ e^{i(m+1)\phi} u_2 \\ e^{im\phi} v_1 \\ e^{i(m+1)\phi} v_2 \end{pmatrix}, \quad (\text{A3})$$

$$J_z \begin{pmatrix} e^{im\phi} u_1 \\ e^{i(m+1)\phi} u_2 \\ e^{im\phi} v_1 \\ e^{i(m+1)\phi} v_2 \end{pmatrix} = m \begin{pmatrix} e^{im\phi} u_1 \\ e^{i(m+1)\phi} u_2 \\ e^{im\phi} v_1 \\ e^{i(m+1)\phi} v_2 \end{pmatrix}, \quad (\text{A4})$$

where we still use the standard Nambu representation $(c_\uparrow, c_\downarrow, c_\downarrow^\dagger, -c_\uparrow^\dagger)$ as in the main text. Denote $\vec{A} = (a_1, \dots, a_N)^T$, $\vec{B} = (b_1, \dots, b_N)^T$, $\vec{C} = (c_1, \dots, c_N)^T$, and $\vec{D} = (d_1, \dots, d_N)^T$, the eigenvalue problem can be expressed as follows:

$$\mathcal{H} \begin{pmatrix} \vec{A} \\ \vec{B} \\ \vec{C} \\ \vec{D} \end{pmatrix} = E \begin{pmatrix} \vec{A} \\ \vec{B} \\ \vec{C} \\ \vec{D} \end{pmatrix}. \quad (\text{A5})$$

Choosing the parameters as follows: $\Delta_0 = 1$ meV, $\eta = 20$ meV, $\xi_0 = 35$ nm, $R = 50\xi_0$, $\alpha = 0.1$ meV, and $\mu = 32$ meV, and using similar cutoff as the vortex pair case, we are able to solve these equations numerically. Note that the Rashba coupling α is sufficient small, therefore it will not change the s -wave superconducting pairing qualitatively.

The energy spectra are shown in Fig. 13, which is consistent with the analytical results for the superconducting gap in Eq. (8). It is easy to calculate the Green's function from the obtained eigenstates, in order to reproduce the BTK theory.

Now we shall calculate the reflection coefficient for the Andreev reflection. To do this, we treat the STM tip as a normal lead, and the Hamiltonian \mathcal{H}_L for this lead reads

$$\mathcal{H}_L = \sum_{i<0,\sigma} \{[-t'\hat{c}_{Li\sigma}^\dagger \hat{c}_{Li+1\sigma} + \text{H.c.}] + [(2t' - \mu')\hat{c}_{Li\sigma}^\dagger \hat{c}_{Li\sigma}]\}. \quad (\text{A6})$$

reads

$$\mathcal{H}_{\text{BdG}} = \left(\frac{\eta}{R^2}L^2 - \frac{\alpha}{R}\vec{L} \cdot \vec{\sigma} - \mu \right) \otimes \tau_z + \Delta_0 I \otimes \tau_x, \quad (\text{A1})$$

which can be written in the form of a 4×4 matrix,

$$\mathcal{H}_{\text{BdG}} = \begin{pmatrix} \Delta_0 & 0 & \Delta_0 & 0 \\ 0 & \Delta_0 & 0 & \Delta_0 \\ -(\frac{\eta}{R^2}L^2 - \mu) + \frac{\alpha}{R}L_z & \frac{\alpha}{R}L_- & -(\frac{\eta}{R^2}L^2 - \mu) + \frac{\alpha}{R}L_z & \frac{\alpha}{R}L_- \\ \frac{\alpha}{R}L_+ & -(\frac{\eta}{R^2}L^2 - \mu) - \frac{\alpha}{R}L_z & \frac{\alpha}{R}L_+ & -(\frac{\eta}{R^2}L^2 - \mu) - \frac{\alpha}{R}L_z \end{pmatrix}. \quad (\text{A2})$$

The coupling between the superconductor (contact point locates in the vortex core center) and the lead Hamiltonian is given by

$$\mathcal{H}_t = \sum_{\sigma} \{t_c \hat{c}_{L0\sigma}^\dagger \hat{c}_{S1\sigma} + \text{H.c.}\}, \quad (\text{A7})$$

where we choose the parameters for the 1D normal Lead (STM tip) as $t' = 25\Delta_0$ and $\mu' = 24\Delta_0$. The coupling constant t_c can be tuned from transparent limit to high-barrier limit.

Using the technique introduced in Sec. IV A, we calculate the Andreev reflection coefficient $T_A = \text{Tr}[\tilde{r}_{he}^\dagger \tilde{r}_{he}]$ for various coupling constants t_c . The numerical results are shown in Figs. 14(a)–14(h). The transparent limit will be taken when $t_c \geq \Delta_0$, while the high-barrier limit occurs at $t_c \ll \Delta_0$.

Now we would like to compare our numerical results with BTK theory for N/I/S junction [26–28]. In the BTK theory, the Andreev reflection coefficient T_A is evaluated through matching boundary condition

$$T_A = \begin{cases} E < \Delta : & \frac{\Delta^2}{E^2 + (\Delta^2 - E^2)(1 + 2Z^2)^2}, \\ E > \Delta : & \frac{u_0^2 v_0^2}{\gamma^2}, \end{cases} \quad (\text{A8})$$

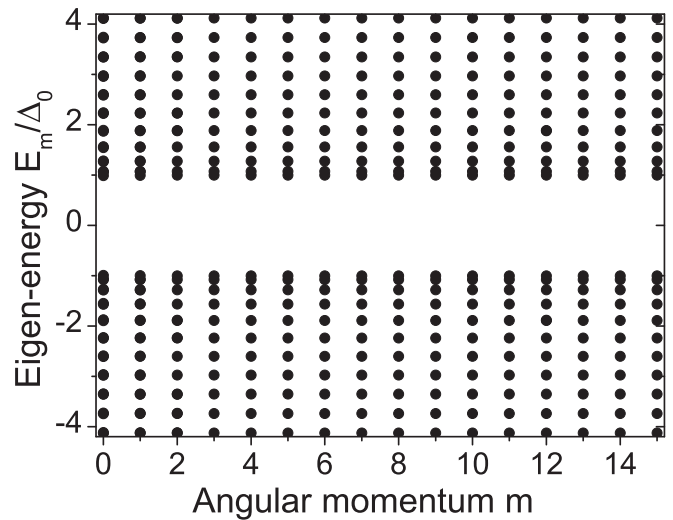


FIG. 13. Energy spectra for the vortex-free case. Only E_m for non-negative angular momentum are calculated numerically and plotted here, with used parameters $\Delta_0 = 1$ meV, $\eta = 20$ meV, $\xi_0 = 35$ nm, $R = 50\xi_0$, $\alpha = 0.1$ meV, and $\mu = 32$ meV.

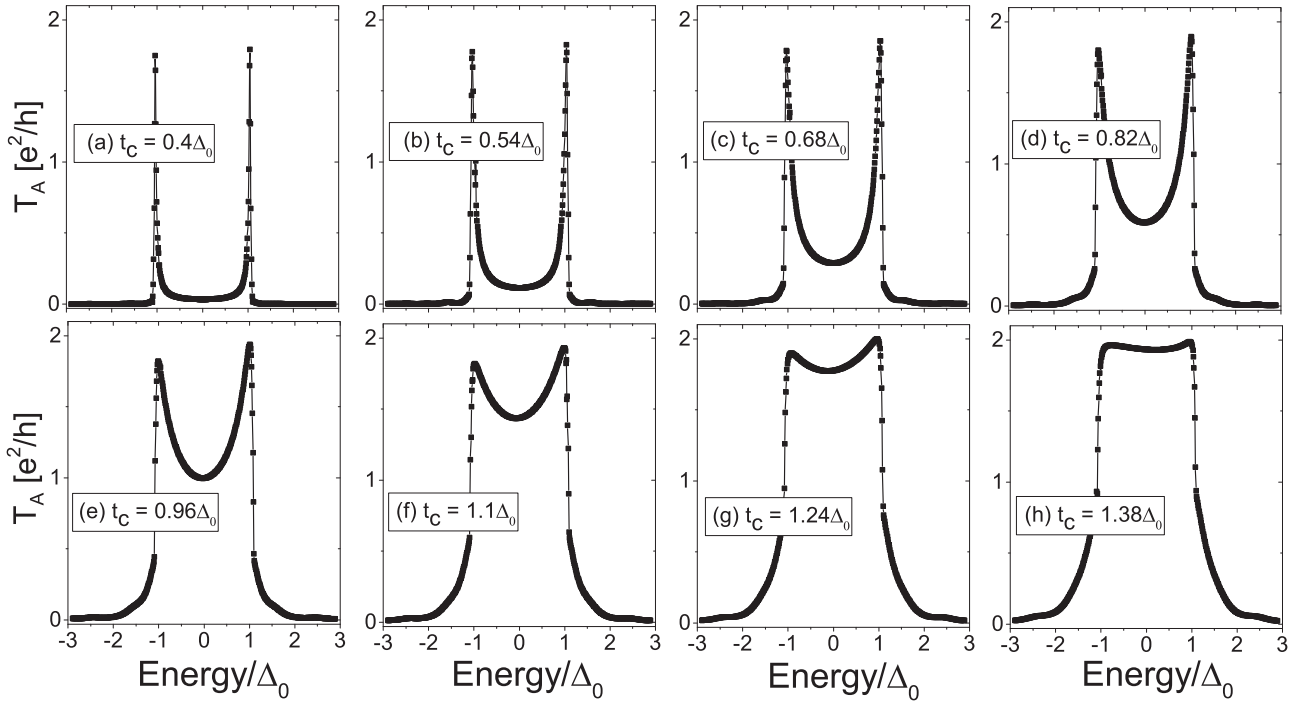


FIG. 14. Ordinary Andreev reflection calculated using $T_A = \text{Tr}[\tilde{r}_{he}^\dagger \tilde{r}_{he}]$ to reproduce the BTK theory (two channels/particles scattering process). Increase the coupling t_c from $0.4\Delta_0$ (high barrier case, large Z) in (a) to $t_c = 1.38\Delta_0$ (transparent limit, tiny Z) in (h).

where $\gamma^2 = u_0^2 + Z^2(u_0^2 - v_0^2)$ and $u_0^2 = 1 - v_0^2 = \frac{1}{2}(1 + \sqrt{\frac{E^2 - \Delta^2}{E^2}})$, and Z is the barrier strength and gives rise to the contact potential $Z\delta(r)$ at the interface between normal metal and superconductor [27]. $Z = 0$ corresponds to the transparent limit, resulting in complete reflection inside the superconducting gap, $T_A(E \leq \Delta) = 1$. On the

contrary, $Z \rightarrow \infty$ corresponds to the high-barrier limit. In this limit, $T_A(E < \Delta) = 0$ but $T_A(E = \Delta) = 1$, namely, Andreev reflection only happens at the edge of the superconducting gap. It is clear that our numerical results reproduce BTK theory well, except the maximum value of T_A is 2 instead of 1. This is because we count two channels in our model.

-
- [1] E. Majorana, *Nuovo Cimento* **14**, 171 (1937).
 [2] A. Y. Kitaev, *Phys. Usp.* **44**, 131 (2001).
 [3] A. Kitaev, *Ann. Phys.* **303**, 2 (2003).
 [4] C. Nayak, S. H. Simon, A. Stern, M. Freedman, and S. Das Sarma, *Rev. Mod. Phys.* **80**, 1083 (2008).
 [5] S. R. Elliott and M. Franz, *Rev. Mod. Phys.* **87**, 137 (2015).
 [6] G. Moore and N. Read, *Nucl. Phys. B* **360**, 362 (1991).
 [7] S. Das Sarma, C. Nayak, and S. Tewari, *Phys. Rev. B* **73**, 220502 (2006).
 [8] L. Fu and C. L. Kane, *Phys. Rev. Lett.* **100**, 096407 (2008).
 [9] Y. Oreg, G. Refael, and F. von Oppen, *Phys. Rev. Lett.* **105**, 177002 (2010).
 [10] R. M. Lutchyn, J. D. Sau, and S. Das Sarma, *Phys. Rev. Lett.* **105**, 077001 (2010).
 [11] J. D. Sau, R. M. Lutchyn, S. Tewari, and S. Das Sarma, *Phys. Rev. Lett.* **104**, 040502 (2010).
 [12] S. Tewari, J. D. Sau, and S. D. Sarma, *Ann. Phys.* **325**, 219 (2010).
 [13] J. Alicea, *Phys. Rev. B* **81**, 125318 (2010).
 [14] T.-P. Choy, J. M. Edge, A. R. Akhmerov, and C. W. J. Beenakker, *Phys. Rev. B* **84**, 195442 (2011).
 [15] S. Nadj-Perge, I. K. Drozdov, B. A. Bernevig, and A. Yazdani, *Phys. Rev. B* **88**, 020407 (2013).
 [16] F. Wilczek, *Nat. Phys.* **5**, 614 (2009).
 [17] V. Mourik, K. Zuo, S. Frolov, S. Plissard, E. Bakkers, and L. Kouwenhoven, *Science* **336**, 1003 (2012).
 [18] M. T. Deng, C. L. Yu, G. Y. Huang, M. Larsson, P. Caroff, and H. Q. Xu, *Nano Lett.* **12**, 6414 (2012).
 [19] A. Das, Y. Ronen, Y. Most, Y. Oreg, M. Heiblum, and H. Shtrikman, *Nat. Phys.* **8**, 887 (2012).
 [20] J. R. Williams and D. Goldhaber-Gordon, *Nat. Phys.* **8**, 778 (2012).
 [21] J.-P. Xu, C. Liu, M.-X. Wang, J. Ge, Z.-L. Liu, X. Yang, Y. Chen, Y. Liu, Z.-A. Xu, C.-L. Gao, D. Qian, F.-C. Zhang, and J.-F. Jia, *Phys. Rev. Lett.* **112**, 217001 (2014).
 [22] S. Nadj-Perge, I. K. Drozdov, J. Li, H. Chen, S. Jeon, J. Seo, A. H. MacDonald, B. A. Bernevig, and A. Yazdani, *Science* **346**, 602 (2014).
 [23] J.-P. Xu, M.-X. Wang, Z. L. Liu, J.-F. Ge, X. Yang, C. Liu, Z. A. Xu, D. Guan, C. L. Gao, D. Qian, Y. Liu, Q.-H. Wang, F.-C. Zhang, Q.-K. Xue, and J.-F. Jia, *Phys. Rev. Lett.* **114**, 017001 (2015).

- [24] M. Kjaergaard, F. Nichele, H. J. Suominen, M. P. Nowak, M. Wimmer, A. R. Akhmerov, J. A. Folk, K. Flensberg, J. Shabani, C. J. Palmström, and C. M. Marcus, *Nat. Commun.* **7**, 12841 (2016).
- [25] J. J. He, T. K. Ng, P. A. Lee, and K. T. Law, *Phys. Rev. Lett.* **112**, 037001 (2014).
- [26] T. M. Klapwijk, G. E. Blonder, and M. Tinkham, *Physica B+C* **109-110**, 1657 (1982).
- [27] S. Kashiwaya and Y. Tanaka, *Rep. Prog. Phys.* **63**, 1641 (2000).
- [28] M. Tinkham, *Introduction to Superconductivity*, 2nd ed. Dover Books on Physics (Courier Corporation, Dover, 2004).
- [29] P. G. De Gennes, *Superconductivity of Metals and Alloys (advanced book classics)* (Addison-Wesley, Redwood City, 1999).
- [30] H.-H. Sun, K.-W. Zhang, L.-H. Hu, C. Li, G.-Y. Wang, H.-Y. Ma, Z.-A. Xu, C.-L. Gao, D.-D. Guan, Y.-Y. Li, C. Liu, D. Qian, Y. Zhou, L. Fu, S.-C. Li, F.-C. Zhang, and J.-F. Jia, *Phys. Rev. Lett.* **116**, 257003 (2016).
- [31] C.-K. Chiu, M. J. Gilbert, and T. L. Hughes, *Phys. Rev. B* **84**, 144507 (2011).
- [32] Y. E. Kraus, A. Auerbach, H. A. Fertig, and S. H. Simon, *Phys. Rev. Lett.* **101**, 267002 (2008).
- [33] Y. E. Kraus, A. Auerbach, H. A. Fertig, and S. H. Simon, *Phys. Rev. B* **79**, 134515 (2009).
- [34] J. D. Sau, S. Tewari, R. M. Lutchyn, T. D. Stanescu, and S. Das Sarma, *Phys. Rev. B* **82**, 214509 (2010).
- [35] J. D. Sau, R. M. Lutchyn, S. Tewari, and S. Das Sarma, *Phys. Rev. B* **82**, 094522 (2010).
- [36] Y. L. Chen, J. G. Analytis, J.-H. Chu, Z. K. Liu, S.-K. Mo, X. L. Qi, H. J. Zhang, D. H. Lu, X. Dai, Z. Fang, S. C. Zhang, I. R. Fisher, Z. Hussain, and Z.-X. Shen, *Science* **325**, 178 (2009).
- [37] H. Zhang, C.-X. Liu, X.-L. Qi, X. Dai, Z. Fang, and S.-C. Zhang, *Nat. Phys.* **5**, 438 (2009).
- [38] M. Cheng, R. M. Lutchyn, V. Galitski, and S. Das Sarma, *Phys. Rev. Lett.* **103**, 107001 (2009).
- [39] J. Zhou, Y.-J. Wu, R.-W. Li, J. He, and S.-P. Kou, *Europhys. Lett.* **102**, 47005 (2013).
- [40] Y. Meir and N. S. Wingreen, *Phys. Rev. Lett.* **68**, 2512 (1992).
- [41] Q.-F. Sun, J. Wang, and T.-H. Lin, *Phys. Rev. B* **59**, 3831 (1999).
- [42] K.-Y. Yang, K. Huang, W.-Q. Chen, T. M. Rice, and F.-C. Zhang, *Phys. Rev. Lett.* **105**, 167004 (2010).
- [43] K. Huang, W.-Q. Chen, T. M. Rice, and F. C. Zhang, *Europhys. Lett.* **99**, 24002 (2012).
- [44] S. Datta, *Electronic Transport in Mesoscopic Systems*, Cambridge Studies in Semiconductor Physics and Microelectronic Engineering (Cambridge University Press, Cambridge, 1997).
- [45] T. Kawakami and X. Hu, *Phys. Rev. Lett.* **115**, 177001 (2015).
- [46] F. Gygi and M. Schlüter, *Phys. Rev. B* **43**, 7609 (1991).
- [47] N. Hayashi, T. Isoshima, M. Ichioka, and K. Machida, *Phys. Rev. Lett.* **80**, 2921 (1998).
- [48] Z.-Z. Li, F.-C. Zhang, and Q.-H. Wang, *Sci. Rep.* **4**, 6363 (2014).
- [49] L. Mao and C. Zhang, *Phys. Rev. B* **82**, 174506 (2010).
- [50] C.-K. Chiu, W. S. Cole, and S. Das Sarma, *Phys. Rev. B* **94**, 125304 (2016).
- [51] K. T. Law, P. A. Lee, and T. K. Ng, *Phys. Rev. Lett.* **103**, 237001 (2009).
- [52] M. Wimmer, A. R. Akhmerov, J. P. Dahlhaus, and C. W. J. Beenakker, *New J. Phys.* **13**, 053016 (2011).
- [53] F. Qu, J. van Veen, F. K. de Vries, A. J. A. Beukman, M. Wimmer, W. Yi, A. A. Kiselev, B.-M. Nguyen, M. Sokolich, M. J. Manfra, F. Nichele, C. M. Marcus, and L. P. Kouwenhoven, [arXiv:1608.05478](https://arxiv.org/abs/1608.05478) [cond-mat.mes-hall].
- [54] F. J. Dyson, *Phys. Rev.* **75**, 1736 (1949).
- [55] R. Landauer, *Philos. Mag.* **21**, 863 (1970).
- [56] D. S. Fisher and P. A. Lee, *Phys. Rev. B* **23**, 6851 (1981).
- [57] M. Büttiker, *Phys. Rev. B* **38**, 9375 (1988).